High-Precision Angle-Resolved Magnetometry with Uniaxial Quantum Centers in Silicon Carbide

D. Simin,[1] F. Fuchs,[1] H. Kraus,[1] A. Sperlich,[1] P. G. Baranov,[2] G. V. Astakhov,[1,*] and V. Dyakonov[1,3,†]
[1] *Experimental Physics VI, Julius-Maximilian University of Würzburg, 97074 Würzburg, Germany*
[2] *Ioffe Physical-Technical Institute, 194021 St. Petersburg, Russia*
[3] *Bavarian Center for Applied Energy Research (ZAE Bayern), 97074 Würzburg, Germany*
(Received 13 February 2015; revised manuscript received 31 May 2015; published 20 July 2015)

We show that uniaxial color centers in silicon carbide with hexagonal lattice structure can be used to measure not only the strength but also the polar angle of the external magnetic field with respect to the defect axis with high precision. The method is based on the optical detection of multiple spin resonances in the silicon vacancy defect with quadruplet ground state and suggests significant improvement of the angle sensitivity compared to spin-1 color centers. We demonstrate a good agreement between the experimental and calculated spin resonance spectra, providing angle resolution better than 1° per $\mathrm{Hz}^{1/2}$ in submillitesla magnetic fields. Our approach is suitable for ensemble as well as single spin-$3/2$ color centers, allowing for angle-resolved magnetometry on the nanoscale at ambient conditions.

DOI: 10.1103/PhysRevApplied.4.014009

I. INTRODUCTION AND MEASUREMENT PRINCIPLE

Optically addressable atomic-scale spin centers constitute a basis for nanomagnetometry with high sensitivity and high spatial resolution [1,2]. The most prominent example is the nitrogen-vacancy (NV) defect in diamond, and several benchmark experiments have been performed using this system [3–5], including proton nuclear-magnetic resonance on the nanometer scale [6,7]. The principle of magnetometry with spin-carrying color centers is based on optical detection of magnetic-resonance (ODMR) frequencies ν subject to an external magnetic field B. In case of individual NV defects with spin $S = 1$, one observes two ODMR lines (ν_1 and ν_2) shifting linearly with the magnetic field as $\pm g_e \mu_B B \cos\theta$, and, hence, the projection of the magnetic field on the defect axis $B\cos\theta$ can be measured.

The NV defect in the diamond cubic lattice is oriented along one out of four $\langle 111 \rangle$ crystallographic axes, and, therefore, using ensemble experiments, the magnetic field vector $\mathbf{B}$ can be reconstructed [8,9]. Ensembles of the NV defects are also suggested [10] for the implementation of high-precision magnetic-field sensors with subpicotesla sensitivity [11] and solid-state frequency standards [12]. These implementations require high homogeneity of the NV centers. The NV defects can be fabricated with preferential alignment [13,14], and in this case, the transverse field component can be reconstructed as well. The ODMR lines also exhibit a quadratic shift because of

$$h\nu_{1,2} \approx h\nu_0 \mp g_e \mu_B B \cos\theta + \xi(\theta) B^2. \tag{1}$$

As the coefficient $\xi(\theta)$ depends on the magnetic-field orientation, the polar angle θ can be measured [4]. However, the angle sensitivity vanishes rapidly in magnetic fields in the submillitesla range as $\delta\theta \propto \nu_0 / B^2$, making the extruction of the polar angle difficult.

Here, we demonstrate an alternative approach to implement angle-resolved magnetometry for submillitesla magnetic fields, which is suitable for ensembles as well as for individual uniaxial spin centers with $S = 3/2$ [15]. In a spin-3/2 system, two extra ODMR lines (ν_3 and ν_4) appear, and in case $g_e \mu_B B \ll h\nu_0$, one can approximate

$$\begin{aligned} h\nu_{1,2} &\approx h\nu_0 \mp g_e \mu_B B f_{\mathrm{in}}(\theta) + \xi_{\mathrm{in}}(\theta) B^2, \\ h\nu_{3,4} &\approx h\nu_0 \mp g_e \mu_B B f_{\mathrm{out}}(\theta) + \xi_{\mathrm{out}}(\theta) B^2, \end{aligned} \tag{2}$$

where $f_{\mathrm{in}}(\theta)$ and $f_{\mathrm{out}}(\theta)$ are particular linearly independent trigonometric functions (Fig. 1) [16]. Therefore, one can measure the quantity $(\nu_2 - \nu_1)/(\nu_4 - \nu_3) = f_{\mathrm{in}}(\theta)/f_{\mathrm{out}}(\theta)$, which is independent of the magnetic-field strength B, thereby allowing us to obtain θ without the need to determine the quadratic shift $\xi(\theta) B^2$.

II. SPIN RESONANCES OF SILICON VACANCIES IN ARBITRARILY ORIENTED MAGNETIC FIELDS

As a model system, we consider a silicon vacancy (V_{Si}) in silicon carbide (SiC) [17–20]. Because of the polymorphism of SiC, there is a large variety of vacancy-related defects with appealing quantum properties confirmed in ensemble [15,16,21–28] as well as in single-defect [29–32] experiments. All measurements presented here are performed at room temperature on a 4*H*-SiC bulk crystal possessing hexagonal lattice structure. The crystal is grown

---

[*] astakhov@physik.uni-wuerzburg.de
[†] dyakonov@physik.uni-wuerzburg.de

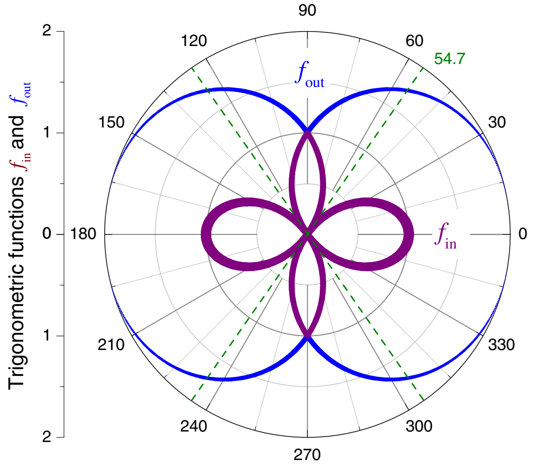

FIG. 1. Polar plot of linearly independent trigonometric functions $f_{\rm in,out}(\theta) = |3\cos\theta \mp \sqrt{1+3\sin^2\theta}|/2$ [16]. The line thicknesses reflect the ODMR contrast of the corresponding spin transitions calculated as explained in the text.

by the standard sublimation technique, such that the [0001] crystallographic direction (c axis) is inclined at an angle of 7° to the surface normal, i.e., to the z axis of the laboratory coordinate system [Fig. 2(a)]. In order to generate $V_{\rm Si}$ defects, the crystal is irradiated with neutrons (5 MeV) with a fluence of 10^{16} cm^{-2}. Their presence is verified by the characteristic photoluminescence (PL) in the near-infrared spectral range [33].

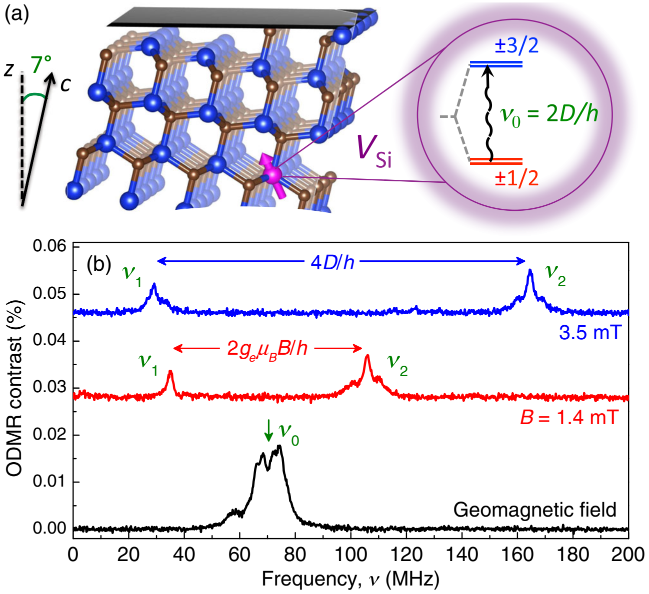

FIG. 2. (a) The c axis of the 4H-SiC crystal is oriented at an angle of 7° with respect to the surface normal. The silicon vacancy $V_{\rm Si}(V2)$ has a spin-3/2 ground state with zero-field splitting $\nu_0 = 70$ MHz. (b) Room-temperature ODMR spectra of the $V_{\rm Si}(V2)$ defect in different magnetic fields applied parallel to the surface normal ($B \| z$).

The $V_{\rm Si}$ defects in hexagonal SiC have a spin-3/2 ground state, which is split in two spin sublevels $m_S = \pm 1/2$ and $m_S = \pm 3/2$ at zero magnetic field [16]. The zero-field splitting $2D$ between these sublevels depends on the lattice site and polytype. In 4H-SiC there are two nonequivalent lattice cites and, hence, two different $V_{\rm Si}$ defects. They are distinguished by their spectroscopic features and labeled as $V1$ and $V2$ centers [18]. Here, we present results for the $V_{\rm Si}(V2)$ center with $2D/h = 70$ MHz [Fig. 2(a)]. A detailed characterization of the system is presented elsewhere [15,16,23,32,33]. Interestingly, $V_{\rm Si}$ can be incorporated into SiC nanocrystals [28], and their density can be controlled over 8 orders of magnitude down to the single-defect level [32].

A laser diode operating at 785 nm is used to optically pump the $V_{\rm Si}(V2)$ center in the host SiC, which has a band gap of 3.23 eV. The optical excitation followed by spin-dependent recombination results in preferential population of the $m_S = \pm 1/2$ sublevels [34,35]. The PL from these centers is passed through 800- and 850-nm long-pass filters and detected by a Si photodiode (up to 1050 nm). The PL intensity is spin dependent; in the case of $V_{\rm Si}(V2)$, it is higher when the system is initialized into the $m_S = \pm 3/2$ states. The radio frequency (rf) provided by a signal generator (2-dBm power) is guided to a thin copper wire and terminated with 50-Ω impedance. The laser beam is focused close to the wire using a 10× optical objective (N.A. = 0.25), and the PL is collected through the sample using a biconvex lens. The x axis of the laboratory coordinate system is set parallel to the wire. The external magnetic field **B** can be applied along arbitrary directions using a 3D coil arrangement. The magnet is calibrated using a 3D Hall sensor providing an angle resolution of 2°.

Without an external magnetic field, a resonance rf $\nu_0 = 2D/h$ induces magnetic dipole transitions between the spin-split sublevels ($\pm 1/2 \to \pm 3/2$) [Fig. 2(a)], resulting in a change of the PL intensity (ΔPL). To increase the sensitivity, the rf is chopped at 677 Hz, and the output PL signal is locked in. An example of the ODMR spectrum (i.e., the ODMR contrast ΔPL/PL versus the applied rf) obtained for $B \to 0$ is shown in Fig. 2(b) (lower curve). The ODMR line is split around $\nu_0 = 70$ MHz due to the geomagnetic and stray magnetic fields.

We now discuss the evolution of the ODMR spectra in external magnetic fields. The corresponding spin Hamiltonian is written in the form

$$\mathcal{H} = g_e \mu_B \mathbf{B} \cdot \mathbf{S} + D[S_z^2 - S(S+1)/3]. \tag{3}$$

Here, $g_e \approx 2.0$ is the electron g factor, μ_B is the Bohr magneton, and S_z is the projection of the total spin on the c axis of 4H-SiC [16]. For the sake of simplicity, we do not consider the hyperfine interaction. We also neglect any deviation from the uniaxial symmetry described by the transverse zero-field splitting parameter $E \ll D$.

Remarkably, the $m_S = \pm 1/2$ ($m_S = \pm 3/2$) states remain doubly degenerated even in the presence of electric and strain fields, in accordance with Kramers theorem. We, hence, take $E = 0$ as a good approximation [16,31].

When an external magnetic field is applied parallel to the symmetry axis $B \| c$ ($\theta = 0°$), the spin states are split as $\epsilon_{\pm 1/2} = -D \pm g_e \mu_B B/2$ and $\epsilon_{\pm 3/2} = +D \pm 3 g_e \mu_B B/2$ [Fig. 3(a)]. One of the dipole-allowed transitions is $(-1/2 \rightarrow -3/2)$ with $\Delta m_S = -1$, and the corresponding ODMR line $\nu_1 = |\nu_0 - g_e \mu_B B/h|$ shifts linearly with the magnetic field, as shown in Fig. 3(c). Another dipole-allowed transition is $(+1/2 \rightarrow +3/2)$ with $\Delta m_S = +1$, and the corresponding ODMR line $\nu_2 = \nu_0 + g_e \mu_B B/h$ shifts linearly towards higher frequencies. For magnetic fields smaller than $B_0 = h\nu_0/(g_e \mu_B) = 2.5$ mT, the splitting between the ODMR lines yields $\nu_2 - \nu_1 = 2 g_e \mu_B B/h$ [middle curve in Fig. 2(b)], and for higher magnetic fields $B > B_0$, this splitting is $\nu_2 - \nu_1 = 4D/h$ [upper curve in Fig. 2(b)]. Remarkably, the dipole-allowed transition $(-1/2 \rightarrow +1/2)$ expected between ν_1 and ν_2 at frequencies $g_e \mu_B B/h$ is not observed in the ODMR spectra. The reason is the equal population of the $m_S = \pm 1/2$ sublevels due to the optical pumping [18].

The behavior becomes much more complex when the magnetic-field vector $\mathbf{B}$ is no longer parallel to the defect symmetry axis. It is instructive to consider a certain pronounced case in detail, namely, when the magnetic field is applied at an angle $\theta = 20°$ with respect to the c axis. By solving Hamiltonian (3), we find the energy level positions and the eigenfunctions $|j\rangle$ ($j = 1, 2, 3, 4$) depending on B [Fig. 3(b)]. The mixing of the $m_S = \pm 1/2$ states in the transverse component of the magnetic field $B \sin\theta$ results in the appearance of two additional ODMR lines, which are labeled ν_3 and ν_4 in Fig. 3(d). The level anticrossing seen in Fig. 3(b) at 1.3 mT (between states $|2\rangle$ and $|3\rangle$) and around 2.0 mT (between states $|1\rangle$ and $|2\rangle$) appears as "turning points" at frequencies $\nu_3^{\mathrm{AC}} = 6$ MHz and $\nu_1^{\mathrm{AC}} = 39$ MHz in the calculated spectra of Fig. 3(d). Furthermore, according to Fig. 3(b), the population of states $|1\rangle$ and $|2\rangle$ becomes equal at 3.0 mT and the ODMR contrast tends to zero, seen as a discontinuity at $\nu_1^Z = 47$ MHz in Fig. 3(d).

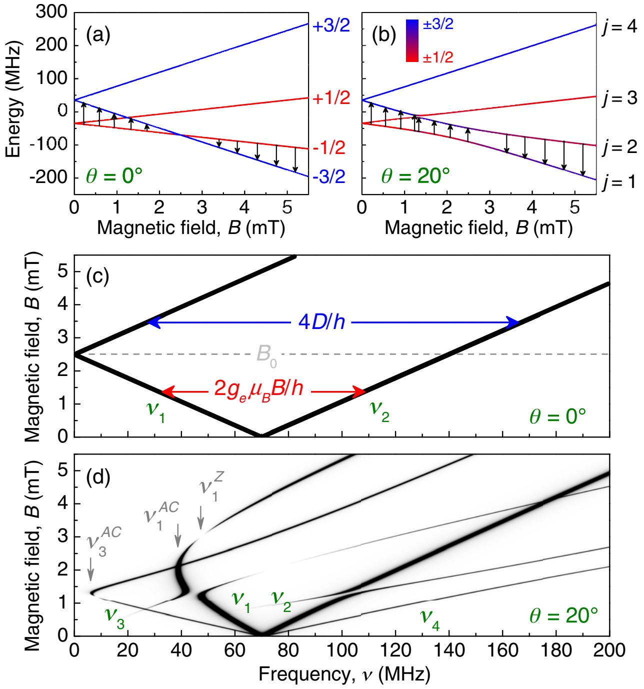

FIG. 3. Spin sublevels in the $V_{\mathrm{Si}}(V2)$ ground state calculated using Hamiltonian (3) as a function of the magnetic field B applied (a) parallel to the c axis and (b) at an angle $\theta = 20°$ with respect to the c axis. Magnetic-field evolution of the ODMR spectrum calculated for (c) $\theta = 0°$ and (d) $\theta = 20°$. The ODMR contrast is coded by the line thickness. The transitions associated with the ν_1 ODMR line are shown by arrows in (a) and (b).

We now explain how the field-dependent ODMR spectra in Fig. 3(d) are calculated. To obtain the probability of the rf-induced transitions between states $|j\rangle$ and $|k\rangle$, we apply

$$W_{jk} \sim |\langle j|\mathbf{B_1} \cdot \mathbf{S_1}|k\rangle|^2. \tag{4}$$

Here, $\mathbf{B_1}$ is the driving rf field (in our experiments $\mathbf{B_1} \| y$). We modify the spin-3/2 matrices $\mathbf{S}_1$ in Eq. (4) to take into account that the $m_S = \pm 1/2$ states are equally populated due to the optical pumping and, hence, do not contribute to the ODMR signal. Namely, the matrix elements coupling these states are set to zero [16]. Finally, we simulate the ODMR spectra assuming Lorentzian line shapes with the experimental value for the full width at half maximum of 2.7 MHz [16]. One can see from Fig. 3(d) that for an arbitrary strength and orientation of the magnetic field, up to six ODMR lines can be observed.

It should be mentioned that, in general, the ODMR contrast depends on decay rates and the optical pumping rate, which are also orientation dependent [36]. In our calculations, we neglect this dependence and obtain the proportionality constant between the rf-induced transition probability of Eq. (4) and the ODMR contrast by comparison with the experiment in a magnetic field of 3.5 mT and a polar angle of 7° [the high-frequency ODMR line in Fig. 2(b)]. The proportionality constant is then fixed for all field orientations and strengths. Within such an approach, we are able to describe many features of the ODMR spectra. Figure 4(a) presents the evolution of the ODMR spectra when the external magnetic field is applied parallel to the z axis of the laboratory coordinate system, i.e., at an angle $\theta = 7°$ with respect to the c axis [see Fig. 2(a)]. Because the deviation from the defect symmetry axis is small, the behavior is very similar to the high-symmetry case ($B \| c$) of Fig. 3(c). The difference is the manifestation of anticrossing ($\nu_1^{\mathrm{AC}} = 13$ MHz) between the ($m_S = -3/2$)-like and ($m_S = -1/2$)-like states at 2.5 mT. Furthermore, in addition to the inner resonances ν_1 and ν_2, the outer

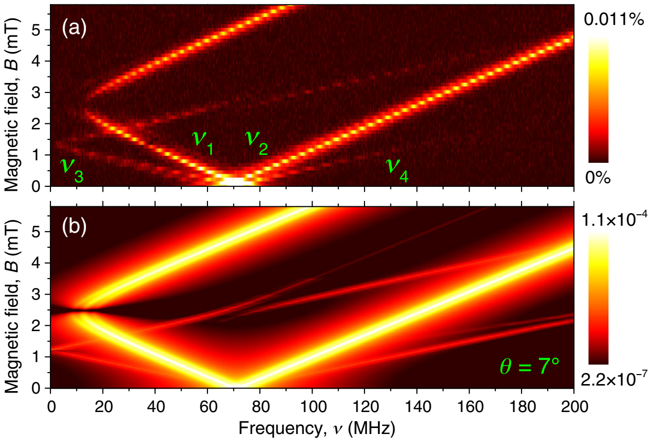

FIG. 4. Evolution of the $V_{\mathrm{Si}}(V2)$ ODMR spectra in magnetic fields applied parallel to the surface normal ($\mathbf{B}\|z$), i.e., at an angle $\theta = 7°$ with respect to the c axis: (a) experiment and (b) calculation. In (b), the ODMR contrast is presented in logarithmic scale to highlight the presence of the outer resonances.

resonances ν_3 and ν_4 appear. They shift with twice the slope of the inner resonances. This behavior is closely reproduced by our calculations shown in Fig. 4(b).

III. EXPERIMENTAL DEMONSTRATION OF ANGLE-RESOLVED MAGNETOMETRY

As another demonstration, we measure the evolution of the ODMR spectra when the external magnetic field is applied in the y-z plane at an angle $\theta' = 60°$ with respect to the z axis [Fig. 5(a)]. This alignment corresponds to the angle $\theta \approx 61°$ between $\mathbf{B}$ and the c axis. It is close to the magic angle $\theta_m = \arccos(1/\sqrt{3}) \approx 54.7°$ when the splitting between the inner ODMR resonances vanishes. Indeed, we experimentally observe $\nu_2 - \nu_1 \ll \nu_4 - \nu_3$ [Fig. 5(b)].

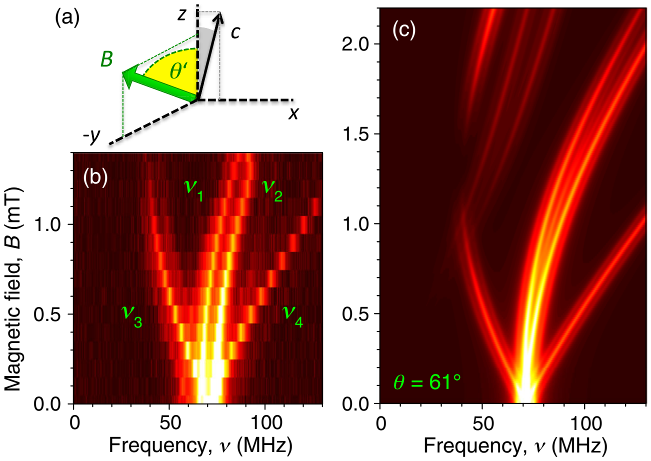

FIG. 5. (a) Evolution of the $V_{\mathrm{Si}}(V2)$ ODMR spectra in magnetic fields applied at an angle $\theta' = 60°$ with respect to the surface normal in the y-z plane: (b) experiment and (c) calculation. The color code of the ODMR contrast in (b) and (c) is the same as in Fig. 4(a).

Furthermore, when the magnetic field is significantly inclined from the symmetry axis, the outer resonances ν_3 and ν_4 become much more pronounced. This complicated behavior is reproduced in the calculated ODMR spectra of Fig. 5(c) as well.

We now discuss how the polar angle of the magnetic field can be reconstructed. Figure 6(a) shows the evolution of the ODMR spectra depending on the magnetic-field orientation at a fixed strength $B = 0.8$ mT. The orientation angle varies from 0° ($\mathbf{B}\|z$) to 90° ($\mathbf{B}\perp z$). As the defect symmetry axis is not exactly parallel to the z axis [the schematic of Fig. 5(a)], there is a difference in the polar angle with respect to the calculated spectra of Fig. 6(b). This angle difference is 7°, as we determine exactly later. As one can see from Figs. 6(a) and 6(b), the splitting between the inner ($\nu_2 - \nu_1$) and outer ($\nu_4 - \nu_3$) resonances changes with magnetic-field orientation. Figure 6(c) represents the interconnection between the polar angle θ, i.e., the angle between the magnetic-field vector and the c axis, and the relative splitting between resonances $\kappa(\theta) = (\nu_2 - \nu_1)/(\nu_4 - \nu_3)$.

Thus, the algorithm to determine the orientation of the magnetic field can be described as follows. For the relatively large polar angles $\theta > 54.7°$, the $m_S = \pm 1/2$

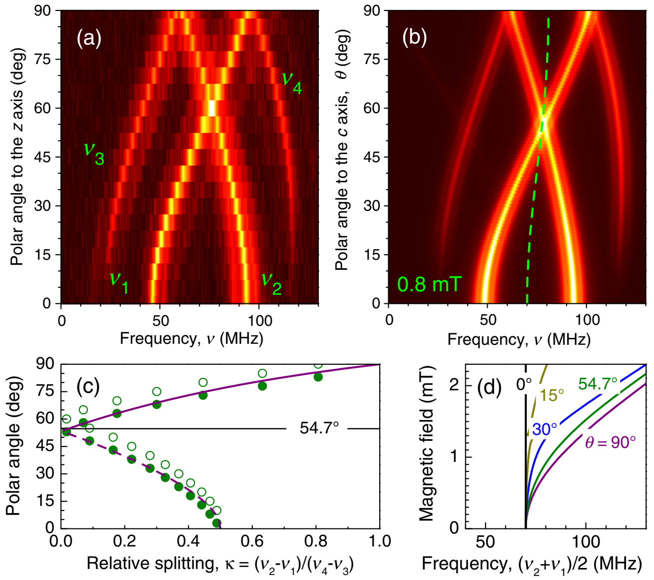

FIG. 6. Angle evolution of the $V_{\mathrm{Si}}(V2)$ ODMR spectra in a magnetic field $B = 0.8$ mT: (a) experiment and (b) calculation. The color code of the ODMR contrast in (a) and (b) is the same as in Fig. 4(a). The dashed line in (b) traces $(\nu_2 + \nu_1)/2$. (c) Polar-angle dependence of the relative splittings between inner $(\nu_2 - \nu_1)$ and outer $(\nu_4 - \nu_3)$ resonances. The dashed line corresponds to the angles when the outer ODMR lines are weak. Open symbols are experimental data from (a). Solid symbols are the same experimental data shifted by 7° to account for the inclination of the c axis with respect to the z axis. (d) Nonlinear shift of the ODMR lines plotted as $(\nu_2 + \nu_1)/2$ against magnetic field for different polar angles.

states are strongly mixed, and the outer resonances are well resolved. To determine θ in this case, one measures the relative distance between the ODMR lines κ and uses the calibration curve shown by the solid line in Fig. 6(c). In the opposite case when $\theta < 54.7°$, the $m_S = \pm 1/2$ states are weakly mixed, and the outer ODMR lines have lower amplitude (less than 50%) compared to the inner ODMR lines. The corresponding calibration curve to determine θ is shown by the dashed line in Fig. 6(c). All in all, the polar angle can be unambiguously derived from the relative positions of the ODMR lines.

To examine this algorithm, we present the measurements of Fig. 6(a) by open symbols in Fig. 6(c). The shift of the experimental data by 7° (solid symbols) results in a perfect agreement with the theoretical curve. Remarkably, this angle coincides with the tilting angle of the c axis with respect to the z axis.

IV. ANGLE RESOLUTION

An important question is the accuracy of the proposed method. First, we discuss the angle resolution $\delta\theta$ due to the nonlinear shift of the ODMR lines as for the NV defects in diamond with $S = 1$ [4]. We take into account the linear and quadratic contributions only, in accordance with Eq. (1). We use the exact solution for the frequencies $\nu_{1,2}$ [4] and obtain to the first order $\xi(\theta) \approx K' g_e^2 \mu_B^2 \sin^2\theta/(h\nu_0)$ with $K' = 3/2$ (Appendix A). The angle resolution is determined by the angle-dependent shift of the spin resonance frequencies at a given magnetic-field strength B as well as by the ODMR linewidth, and, hence, it can be directly linked to the field resolution δB as (Appendix A)

$$\delta\theta_{S=1}(\theta) \approx \frac{180}{\pi}\frac{1}{K' \sin 2\theta}\frac{h\nu_0}{g_e\mu_B B}\frac{\delta B}{B}. \qquad (5)$$

Here, $\delta\theta$ is given in degrees. Remarkably, for magnetic fields below $B_c \approx \sqrt{h\nu_0 \delta B/(\sqrt{\tau} 3\pi g_e \mu_B)}$ (τ is the integration time), the field orientation cannot be resolved using this method. For instance, in the NV defects $\nu_0 = D/h = 2.87$ GHz, and taking a dc field resolution $\delta B = 10\ \mu\mathrm{T}/\sqrt{\mathrm{Hz}}$, we obtain for $\tau = 1$ s the critical field $B_c \approx 0.3$ mT.

An obvious solution to increase the angle resolution is to use defects with smaller D. The $V_{\mathrm{Si}}(V2)$ in SiC has $\nu_0 = 2D/h = 70$ MHz, and the critical magnetic field $B_c \approx 0.05$ mT is obtained using Eq. (5) with the same values of δB and τ as in the previous case. This is illustrated in Fig. 6(d), where the mean value $(\nu_2 + \nu_1)/2 \approx \nu_0 + \xi(\theta)B^2$ is calculated using Eq. (3) and plotted versus the magnetic-field strength for different polar angles. Indeed, for $B < 0.1$ mT, the mean values are hardly distinguishable. For $B = 0.8$ mT, the quadratic shift $\xi(\theta)B^2$ becomes detectable [the dashed line in Fig. 6(b)], allowing us to resolve the magnetic-field orientation.

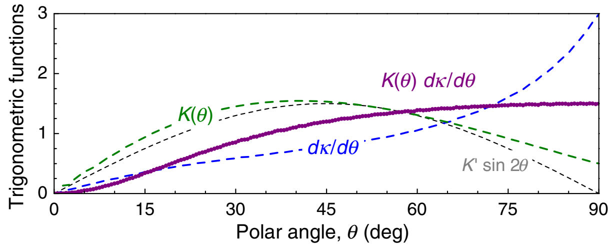

FIG. 7. Field-independent trigonometric functions $K' \sin 2\theta$, $K(\theta)$, and $d\kappa(\theta)/d\theta$ to estimate the polar-angle resolution, according to Eq. (5) and Eq. (6).

We now consider the method to measure the polar angle described in the present paper. As in the previous case, the angle resolution can be directly linked to the field resolution as (Appendix B)

$$\delta\theta_{S=3/2}(\theta) \approx \frac{180}{\pi}\frac{1}{K(\theta)|d\kappa(\theta)/d\theta|}\frac{\delta B}{B}. \qquad (6)$$

Here, $K(\theta)$ describes the experimental accuracy to measure $\kappa(\theta)$. Comparing to Eq. (5), the term $h\nu_0/(g_e\mu_B B)$ is absent, and the angle resolution can be significantly improved in weak magnetic fields. We calculate the field-independent trigonometric functions $K(\theta)$ and $d\kappa(\theta)/d\theta$, as presented in Fig. 7. In the most sensitive case of $\theta \to 90°$, these functions take values $K(\theta) = 0.5$ and $d\kappa(\theta)/d\theta = 3$, and we obtain for $B = 0.8$ mT the angle resolution $\delta\theta \sim 0.5°/\sqrt{\mathrm{Hz}}$, assuming in our experiments $\delta B \approx 10\ \mu\mathrm{T}/\sqrt{\mathrm{Hz}}$ [16]. For small angles $\theta < 20°$, the resolution becomes significantly lower. Remarkably, for $\theta \to 0°$, the outer resonances disappear, and the polar-angle resolution can be estimated from $\delta\theta(\Delta\theta) = \Delta\theta$, yielding $\delta\theta \sim 9°/\sqrt{\mathrm{Hz}}$ in this case. Further improvement is possible by using advanced read-out protocols [2].

V. SUMMARY

Uniaxial spin-3/2 centers in a hexagonal lattice can be used to measure the magnetic-field strength and to reconstruct the magnetic-field orientation with respect to the symmetry axis of the crystal (i.e., the polar angle). The method is based on the ODMR technique and is applicable for ensembles of spin centers as well as for single centers. As a probe, we use the V_{Si} spin center in 4H-SiC, and the polar-angle resolution of about $1°/\sqrt{\mathrm{Hz}}$ is demonstrated in submillitesla magnetic fields. The experiments are very well described by our model for any magnetic-field orientation. It should be mentioned that this method does not provide information about the azimuthal angle, but this can potentially be overcome by using differently oriented centers, for instance, along the c axis and in the basal plane of the crystal. The selective optical addressability [23] and coherent control [22] of single-V_{Si} centers [31] are reported. The combination of these capabilities with our findings suggests promising perspectives for vector magnetometry and local imaging down to the nanoscale.

ACKNOWLEDGMENTS

This work is supported by the German Research Foundation (DFG) under Grant No. AS 310/4 as well as by the RFBR (Grant No. 14-02-91344) and by the RMES (Grant No. 14.604.21.0083). H. K. acknowledges the support of the German Academic Exchange Service (DAAD), with funds of the German Federal Ministry of Education and Research (BMBF) and EU Marie Curie Actions (DAAD P. R. I. M. E. Project No. 57183951).

Note added.—Recently, theoretical aspects of silicon-carbide-based vector magnetometry have been posted in Ref. [37], which are in accordance with our experimental findings and clearly depict the high potential of this spin system.

APPENDIX A: ESTIMATION OF THE ANGLE RESOLUTION FOR A SPIN-1 SYSTEM

Following Eq. (1), the difference and the product of the ODMR frequencies can be expressed in the form

$$h\nu_2 - h\nu_1 = 2\beta\cos\theta \tag{A1}$$

and

$$h^2\nu_2\nu_1 = (D + \xi B^2)^2 - (\beta\cos\theta)^2, \tag{A2}$$

with $\beta = g_e\mu_B B$ and $D = h\nu_0$. Using $3\beta^2 = (h\nu_2 - h\nu_1)^2 + h^2\nu_2\nu_1 - D^2$ [4], we obtain assuming $\xi B^2 \ll D$,

$$\xi(\theta) \approx \frac{3g_e^2\mu_B^2\sin^2\theta}{2D}. \tag{A3}$$

The polar angle θ can be reconstructed by analyzing the angle-dependent shift of the mean value at a given magnetic-field strength $h(\nu_2 + \nu_1)/2 = h\tilde{\nu} \approx D + \xi(\theta)B^2$. The angle resolution $\delta\theta$ is, hence, determined by the accuracy to measure the frequency shift $\delta\tilde{\nu}$,

$$\delta\theta = \frac{1}{|d\tilde{\nu}(\theta)/d\theta|}\delta\tilde{\nu} = \frac{2D}{3g_e^2\mu_B^2B^2\sin 2\theta}\delta\tilde{\nu}. \tag{A4}$$

As $\delta\tilde{\nu}$ is directly linked to the magnetic-field sensitivity $\delta\tilde{\nu} = g_e\mu_B\delta B/h$, we obtain Eq. (5) in the main text after conversion from radians to degrees.

APPENDIX B: ESTIMATION OF THE ANGLE RESOLUTION FOR A SPIN-3/2 SYSTEM

The angle resolution $\delta\theta$ is determined in this case by the accuracy to measure the ratio between the frequency shifts of the inner and outer resonances $\delta\kappa$,

$$\delta\theta = \frac{1}{|d\kappa(\theta)/d\theta|}\delta\kappa. \tag{B1}$$

Following Eq. (2), $\nu_2 - \nu_1 = \nu_{\mathrm{in}} = 2f_{\mathrm{in}}(\theta)g_e\mu_B B/h$ and $\nu_4 - \nu_3 = \nu_{\mathrm{out}} = 2f_{\mathrm{out}}(\theta)g_e\mu_B B/h$ [16] and as $\kappa = \nu_{\mathrm{in}}/\nu_{\mathrm{out}}$, and, consequently,

$$\delta\kappa = \sqrt{\left(\frac{\delta\nu_{\mathrm{in}}}{\nu_{\mathrm{out}}}\right)^2 + \left(\frac{\nu_{\mathrm{in}}\delta\nu_{\mathrm{out}}}{\nu_{\mathrm{out}}^2}\right)^2}, \tag{B2}$$

we obtain using $\delta\nu_{\mathrm{in,out}} = 2g_e\mu_B\delta B/\sqrt{h^2K_{\mathrm{in,out}}}$,

$$\delta\kappa = \frac{\delta B}{B}\sqrt{\left(\frac{1}{f_{\mathrm{out}}}\right)^2\frac{1}{K_{\mathrm{in}}} + \left(\frac{f_{\mathrm{in}}}{f_{\mathrm{out}}^2}\right)^2\frac{1}{K_{\mathrm{out}}}}. \tag{B3}$$

Here, $K_{\mathrm{in}}(\theta)$ and $K_{\mathrm{out}}(\theta)$ are relative ODMR contrasts with respect to the case of $\theta = 0°$, for instance, $K_{\mathrm{in}}(0°) = 1$ and $K_{\mathrm{out}}(0°) = 0$. With

$$\frac{1}{K(\theta)} = \sqrt{\left(\frac{1}{f_{\mathrm{out}}}\right)^2\frac{1}{K_{\mathrm{in}}} + \left(\frac{f_{\mathrm{in}}}{f_{\mathrm{out}}^2}\right)^2\frac{1}{K_{\mathrm{out}}}}, \tag{B4}$$

we obtain Eq. (6) in the main text after conversion from radians to degrees.

[1] B. M. Chernobrod and G. P. Berman, Spin microscope based on optically detected magnetic resonance, J. Appl. Phys. **97**, 014903 (2005).

[2] J. M. Taylor, P. Cappellaro, L. Childress, L. Jiang, D. Budker, P. R. Hemmer, A. Yacoby, R. Walsworth, and M. D. Lukin, High-sensitivity diamond magnetometer with nanoscale resolution, Nat. Phys. **4**, 810 (2008).

[3] J. R. Maze, P. L. Stanwix, J. S. Hodges, S. Hong, J. M. Taylor, P. Cappellaro, L. Jiang, M. V. Gurudev Dutt, E. Togan, A. S. Zibrov, A. Yacoby, R. L. Walsworth, and M. D. Lukin, Nanoscale magnetic sensing with an individual electronic spin in diamond, Nature (London) **455**, 644 (2008).

[4] G. Balasubramanian, I. Y. Chan, R. Kolesov, M. Al-Hmoud, J. Tisler, C. Shin, C. Kim, A. Wojcik, P. R. Hemmer, A. Krueger, T. Hanke, A. Leitenstorfer, R. Bratschitsch, F. Jelezko, and J. Wrachtrup, Nanoscale imaging magnetometry with diamond spins under ambient conditions, Nature (London) **455**, 648 (2008).

[5] C. Degen, Christian Degen, Nanoscale magnetometry: Microscopy with single spins, Nat. Nanotechnol. **3**, 643 (2008).

[6] H. J. Mamin, M. Kim, M. H. Sherwood, C. T. Rettner, K. Ohno, D. D. Awschalom, and D. Rugar, Nanoscale nuclear magnetic resonance with a nitrogen-vacancy spin sensor, Science **339**, 557 (2013).

[7] T. Staudacher, F. Shi, S. Pezzagna, J. Meijer, J. Du, C. A. Meriles, F. Reinhard, and J. Wrachtrup, Nuclear magnetic resonance spectroscopy on a (5-nanometer) 3 sample volume, Science **339**, 561 (2013).

[8] B. J. Maertz, A. P. Wijnheijmer, G. D. Fuchs, M. E. Nowakowski, and D. D. Awschalom, Vector magnetic field microscopy using nitrogen vacancy centers in diamond, Appl. Phys. Lett. **96**, 092504 (2010).

[9] S. Steinert, F. Dolde, P. Neumann, A. Aird, B. Naydenov, G. Balasubramanian, F. Jelezko, and J. Wrachtrup, High sensitivity magnetic imaging using an array of spins in diamond, Rev. Sci. Instrum. **81**, 043705 (2010).

[10] V. Acosta, E. Bauch, M. Ledbetter, C. Santori, K. M. Fu, P. Barclay, R. Beausoleil, H. Linget, J. Roch, F. Treussart, S. Chemerisov, W. Gawlik, and D. Budker, Diamonds with a high density of nitrogen-vacancy centers for magnetometry applications, Phys. Rev. B **80**, 115202 (2009).

[11] T. Wolf, P. Neumann, K. Nakamura, H. Sumiya, J. Isoya, and J. Wrachtrup, A subpicotesla diamond magnetometer, arXiv:1411.6553.

[12] J. S. Hodges, N. Y. Yao, D. Maclaurin, C. Rastogi, M. D. Lukin, and D. Englund, Timekeeping with electron spin states in diamond, Phys. Rev. A **87**, 032118 (2013).

[13] J. Michl, T. Teraji, S. Zaiser, I. Jakobi, G. Waldherr, F. Dolde, P. Neumann, M. W. Doherty, N. B. Manson, J. Isoya, and J. Wrachtrup, Perfect alignment and preferential orientation of nitrogen-vacancy centers during chemical vapor deposition diamond growth on (111) surfaces, Appl. Phys. Lett. **104**, 102407 (2014).

[14] M. Lesik, J. P. Tetienne, A. Tallaire, J. Achard, V. Mille, A. Gicquel, J. F. Roch, and V. Jacques, Perfect preferential orientation of nitrogen-vacancy defects in a synthetic diamond sample, Appl. Phys. Lett. **104**, 113107 (2014).

[15] H. Kraus, V. A. Soltamov, D. Riedel, S. Väth, F. Fuchs, A. Sperlich, P. G. Baranov, V. Dyakonov, and G. V. Astakhov, Room-temperature quantum microwave emitters based on spin defects in silicon carbide, Nat. Phys. **10**, 157 (2014).

[16] H. Kraus, V. A. Soltamov, F. Fuchs, D. Simin, A. Sperlich, P. G. Baranov, G. V. Astakhov, and V. Dyakonov, Magnetic field and temperature sensing with atomic-scale spin defects in silicon carbide, Sci. Rep. **4**, 5303 (2014).

[17] V. S. Vainer and V. A. Il'in, Electron spin resonance of exchange-coupled vacancy pairs in hexagonal silicon carbide, Sov. Phys. Solid State **23**, 2126 (1981).

[18] E. Sörman, N. Son, W. Chen, O. Kordina, C. Hallin, and E. Janzén, Silicon vacancy related defect in $4H$ and $6H$ SiC, Phys. Rev. B **61**, 2613 (2000).

[19] N. Mizuochi, S. Yamasaki, H. Takizawa, N. Morishita, T. Ohshima, H. Itoh, and J. Isoya, Continuous-wave and pulsed EPR study of the negatively charged silicon vacancy with $S = 3/2$ and C_{3v} symmetry in n-type $4H$-SiC, Phys. Rev. B **66**, 235202 (2002).

[20] P. G. Baranov, A. P. Bundakova, A. A. Soltamova, S. B. Orlinskii, I. V. Borovykh, R. Zondervan, R. Verberk, and J. Schmidt, Silicon vacancy in SiC as a promising quantum system for single-defect and single-photon spectroscopy, Phys. Rev. B **83**, 125203 (2011).

[21] W. F. Koehl, B. B. Buckley, F. Joseph Heremans, G. Calusine, and D. D. Awschalom, Room temperature coherent control of defect spin qubits in silicon carbide, Nature (London) **479**, 84 (2011).

[22] V. A. Soltamov, A. A. Soltamova, P. G. Baranov, and I. I. Proskuryakov, Room Temperature Coherent Spin Alignment of Silicon Vacancies in $4H$- and $6H$-SiC, Phys. Rev. Lett. **108**, 226402 (2012).

[23] D. Riedel, F. Fuchs, H. Kraus, S. Väth, A. Sperlich, V. Dyakonov, A. Soltamova, P. Baranov, V. Ilyin, and G. V. Astakhov, Resonant Addressing and Manipulation of Silicon Vacancy Qubits in Silicon Carbide, Phys. Rev. Lett. **109**, 226402 (2012).

[24] F. Fuchs, V. A. Soltamov, S. Väth, P. G. Baranov, E. N. Mokhov, G. V. Astakhov, and V. Dyakonov, Silicon carbide light-emitting diode as a prospective room temperature source for single photons, Sci. Rep. **3**, 1637 (2013).

[25] A. L. Falk, B. B. Buckley, G. Calusine, W. F. Koehl, V. V. Dobrovitski, A. Politi, C. A. Zorman, P. X. L. Feng, and D. D. Awschalom, Polytype control of spin qubits in silicon carbide, Nat. Commun. **4**, 1819 (2013).

[26] P. V. Klimov, A. L. Falk, B. B. Buckley, and D. D. Awschalom, Electrically Driven Spin Resonance in Silicon Carbide Color Centers, Phys. Rev. Lett. **112**, 087601 (2014).

[27] A. L. Falk, P. V. Klimov, B. B. Buckley, V. Ivády, I. A. Abrikosov, G. Calusine, W. F. Koehl, A. Gali, and D. D. Awschalom, Electrically and Mechanically Tunable Electron Spins in Silicon Carbide Color Centers, Phys. Rev. Lett. **112**, 187601 (2014).

[28] A. Muzha, F. Fuchs, N. V. Tarakina, D. Simin, M. Trupke, V. A. Soltamov, E. N. Mokhov, P. G. Baranov, V. Dyakonov, A. Krueger, and G. V. Astakhov, Room-temperature near-infrared silicon carbide nanocrystalline emitters based on optically aligned spin defects, Appl. Phys. Lett. **105**, 243112 (2014).

[29] S. Castelletto, B. C. Johnson, V. Ivády, N. Stavrias, T. Umeda, A. Gali, and T. Ohshima, A silicon carbide room-temperature single-photon source, Nat. Mater. **13**, 151 (2013).

[30] D. J. Christle, A. L. Falk, P. Andrich, P. V. Klimov, J. ul Hassan, N. T. Son, E. Janzén, T. Ohshima, and D. D. Awschalom, Isolated electron spins in silicon carbide with millisecond coherence times, Nat. Mater. **14**, 160 (2015).

[31] M. Widmann, S.-Y. Lee, T. Rendler, N. Tien Son, H. Fedder, S. Paik, L.-P. Yang, N. Zhao, S. Yang, I. Booker, A. Denisenko, M. Jamali, S. Ali Momenzadeh, I. Gerhardt, T. Ohshima, A. Gali, E. Janzén, and J. Wrachtrup, Coherent control of single spins in silicon carbide at room temperature, Nat. Mater. **14**, 164 (2015).

[32] F. Fuchs, B. Stender, M. Trupke, D. Simin, J. Pflaum, V. Dyakonov, and G. V. Astakhov, Engineering near-infrared single-photon emitters with optically active spins in ultrapure silicon carbide, Nat. Commun. **6**, 7578 (2015).

[33] T. C. Hain, F. Fuchs, V. A. Soltamov, P. G. Baranov, G. V. Astakhov, T. Hertel, and V. Dyakonov, Excitation and recombination dynamics of vacancy-related spin centers in silicon carbide, J. Appl. Phys. **115**, 133508 (2014).

[34] P. G. Baranov, A. P. Bundakova, I. V. Borovykh, S. B. Orlinskii, R. Zondervan, and J. Schmidt, Spin polarization induced by optical and microwave resonance radiation in a Si vacancy in SiC: A promising subject for the spectroscopy of single defects, J. Exp. Theor. Phys. Lett. **86**, 202 (2007).

[35] J. Isoya, T. Umeda, N. Mizuochi, N. T. Son, E. Janzén, and T. Ohshima, EPR identification of intrinsic defects in SiC, Phys. Status Solidi (b) **245**, 1298 (2008).

[36] J. P. Tetienne, L. Rondin, P. Spinicelli, M. Chipaux, T. Debuisschert, J. F. Roch, and V. Jacques, Magnetic-field-dependent photodynamics of single NV defects in diamond: An application to qualitative all-optical magnetic imaging, New J. Phys. **14**, 103033 (2012).

[37] S.-Y. Lee, M. Niethammer, and J. Wrachtrup, Vector magnetometery based on $S = 3/2$ electronic spins, arXiv:1505.06914.